IOP Conference Series: Materials Science and Engineering

PAPER • **OPEN ACCESS**

Control of crystallographic textures by metal additive manufacturing-A review

To cite this article: Takayoshi Nakano 2024 *IOP Conf. Ser.: Mater. Sci. Eng.* **1310** 012013

IOP Conf. Series: Materials Science and Engineering **1310** (2024) 012013 doi:10.1088/1757-899X/1310/1/012013

Control of crystallographic textures by metal additive manufacturing – A review

Takayoshi Nakano[1,2*]

[1] Division of Materials and Manufacturing Science, Graduate School of Engineering, Osaka University, Suita, Japan
[2] Anisotropic Design and Additive Manufacturing Research Center, Osaka University, Suita, Japan

[*]E-mail: nakano@mat.eng.osaka-u.ac.jp

Abstract. Metal additive manufacturing (AM), a unique manufacturing method that stacks powder materials layer-by-layer to fabricate products with complex shapes and high precision, allows for a wide range of control over metallurgical microstructures. Metal AM defines solidification units with specific solidification directions and fast cooling, thereby enabling the control of the resulting metallurgical microstructure. However, the studies investigated texture control and utilizing textured microstructure are lacking in the literature. This review describes some of the results of our research on the control of crystallographic textures by laser powder bed fusion (LPBF), focusing on (1) the effect of powder properties on densification and crystallographic texture formation, (2) the effect of the melt pool shape and crystallographic characteristics of the starting material on the formation and orientation of single crystals, and (3) the successful application of alloy design to the preparation of highly functional single-crystalline-like textured biological high-entropy alloys considering specific solidification fields under LPBF.

1. Overview

The basic concept of additive manufacturing (AM) is the fabrication of three-dimensional parts in a two-dimensional plane using a layer-by-layer approach [1]. In 2013, over 30 years after the concept was first introduced, former US President Barack Obama suggested that "3D printing has the potential to revolutionize the way we make almost everything." Indeed, the number of academic publications on AM has increased annually (figure 1, red columns), conferences and research groups on AM have been established in many countries, and several exhibitions and international conferences have been held. In recent years, the market for AM has rapidly increased worldwide.

Metal AM is expected to be applicable to a wide range of industries, including aerospace, automotive manufacturing, energy, chemicals, medical/healthcare, and consumer products. When combined with topology optimization technology, AM may be able to overcome several issues often encountered in conventional subtractive manufacturing, such as the manufacture of complex shapes, flexible customization of structures, and significant reductions in weight, while maintaining the required strength under specific mechanical environments. The significance of

and expectations for the social implementation of AM are important from the viewpoint of realizing a carbon-neutral society.

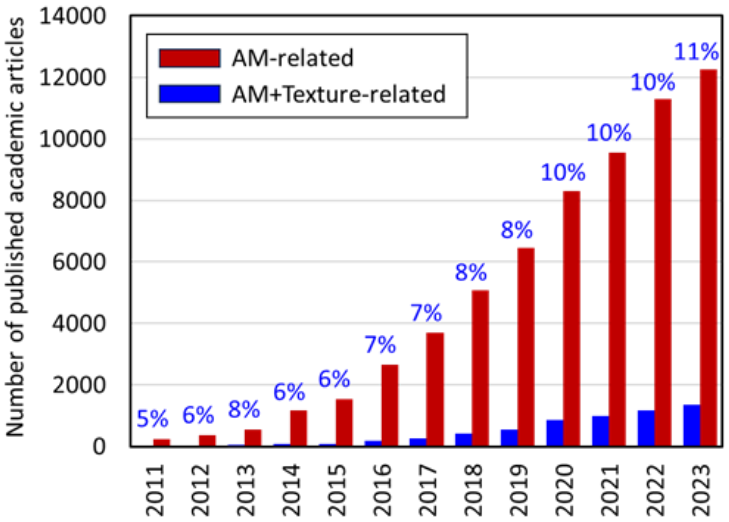

Figure 1. Trends of publications on additive manufacturing (AM) in general (red) and those focusing on texture-related AM research (blue). We searched for publications containing the phrase "additive manufacturing" in their title, abstract, and keywords for the former and those containing "additive manufacturing" AND texture OR orientation for the latter in Scopus on April 13, 2024. The numbers at the top the red columns indicate the percentage of texture-related publications relative to the number of AM publications for the given year.

AM, especially powder bed fusion (PBF), which uses fine powder as the starting material, was originally developed to fabricate complex three-dimensional shapes with high precision. In recent years, however, the importance of the characteristics of the metallic material, rather than its shape, has gradually been recognized. For example, alloy design, which involves the design of alloys that support various conditions inherent to AM, such as ultrarapid melting and solidification, layer-by-layer manufacturing, and the occurrence of thermal and residual stresses, is expected to become a major trend in future AM research [2].

Our research group has focused on material microstructures exhibiting anisotropic characteristics, including cubic or fiber texture formations, as a material property of metals, and has been conducting research aimed at the artificial control of such microstructures [3, 4]. In 2017, we successfully formed a single-crystalline-like highly oriented microstructure and controlled its orientation using different laser scanning strategies [3, 4]. Since then, we have developed a new method for controlling the orientation of crystals in various metals and alloys [5]. We previously investigated crystallographic textures and the control of mechanical properties based on crystal orientation in various metal and alloy systems [5, 6]. As shown in figure 1, the proportion of publications on crystalline microstructures in relation to AM has steadily increased in recent years, reaching 11% in 2023. Thus, the control of crystallographic textures may be considered one of the most important and popular research topics in AM today., of which there are still challenges to control the texture of metal materials with different crystal structures.

This review presents some of the results of our research on metal AM, focusing on the crystallographic textures produced by laser PBF (LPBF) as a powder-based process. Specifically, this article discusses: (1) the effect of powder properties on densification, which is essential for the formation of crystallographic textures, (2) the effect of the melt pool shape and

crystallographic characteristics of the starting material on the formation and orientation of single crystals, and (3) the successful application of alloy design for the formation of single crystals in biological high-entropy alloys (BioHEAs) by LPBF.

2. Importance of powder properties to composite quality

Material microstructures with anisotropic properties, that is, exhibiting crystallographic textures, are formed via epitaxial growth between adjacent scan tracks and subsequent melt pool layers. Therefore, obtaining a dense compact is essential to control crystal growth. Similar to that in other powder metallurgical methods [7,8], the properties of the starting powder material also influence the process performance and quality of products fabricated using the PBF method [9]. In particular, for difficult-to-print materials, the properties of the powder have a pronounced influence on product quality.

Figure 2 shows SEM images of tungsten powders prepared by (a) crushing, (b) gas atomization, and (c) plasma atomization. The particle size distributions of these particles were analyzed by laser diffraction, and the results are shown in figure 2(d). Tungsten solidifies rapidly owing to its extremely high melting point (3422 °C), high thermal conductivity, and high melt viscosity [10, 11], rendering PBF processing challenging. The crushed powder particles are polygonal in shape and agglomerate to form secondary particles, whereas the atomized powder particles are generally spherical. Notably, the plasma-atomized powder particles are nearly spherical in shape, with hardly any satellite particles [12].

According to the results of analyses of the particle size distribution, powder bed density, and powder flowability characteristics of the tungsten powders (table 1), plasma-atomized powders have a high powder bed density and excellent flowability (Hauser ratio = tapped density/bulk density close to 1, with a small avalanche angle, angle of repose, and surface fractal). In other words, plasma-atomized powders form highly dense and uniform powder beds [12].

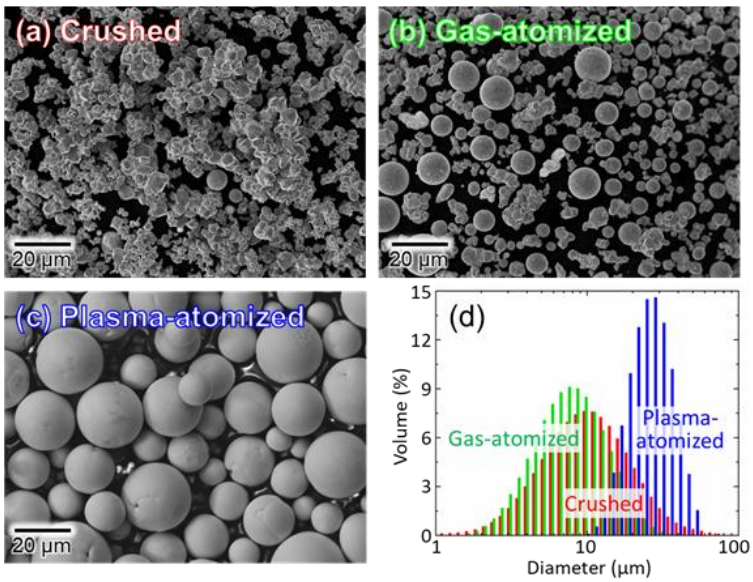

Figure 2. Morphology of (a) crushed, (b) gas-atomized, and (c) plasma-atomized tungsten powders. (d) Particle size distributions of the tungsten powders. Adapted with modifications from reference [12], published under the CC-BY-4.0 license.

Table 1. Size distribution, density, and flowability of crushed, gas-atomized, and plasma-atomized tungsten powders. Adapted with modifications from reference [12], published under the CC-BY-4.0 license.

Property	Crushed	Gas-atomized	Plasma-atomized
D10 (μm)	4.5	4.1	17.7
D50 (μm)	10.7	8.3	27.4
D90 (μm)	24.6	16.5	41.8
Bulk density (g/mL)	3.61	7.50	13.64
Tapped density (g/mL)	4.84	9.09	15.00
Hauser ratio	1.34	1.21	1.10
Avalanche angle (deg.)	59.3	47.9	32.4
Angle of repose (deg.)	41.3	40.4	25.5
Surface fractal	4.25	2.99	2.21

Figure 3(a) shows the relative densities of the products fabricated using the three types of tungsten powders depending on the laser energy density. SEM images of the cross-section of the products prepared at a laser energy density of 375 J/mm^3 (laser power = 360 W, scanning speed = 600 mm/s, hatch spacing = 0.08 mm, layer thickness = 0.02 mm) and their Vickers hardness are shown in figure 3(b–d). The densities of the products depend on the properties of the starting powders, with plasma-atomized powders consistently exhibiting the highest densities. Macroscopic defects, such as large lack of fusion regions, attributed to a low powder bed density are observed in the crushed powders, resulting in low hardness in the final product. By contrast, macrodefects are almost nonexistent in the atomized powders but cracks parallel to the building direction (BD) are formed, preventing densification [12]. As shown in figure 4, cracks parallel to the BD are formed at the center of the melt pool, where <100>//BD-oriented grains extending in the BD are found, resulting straight high-angle grain boundaries which are stated to be sensitive for crack initiation and propagation due to residual stress during fast solidification [12]. These cracks are located at high-angle grain boundaries on both sides of the <100>//BD grains. The formation of a crystallographic lamellar microstructure in which <100>//BD grains extend in the BD has been reported for SUS316L stainless steel [13, 15] and nickel-based alloys [16,1 7]. This phenomenon has been shown to occur when the radius of curvature at the bottom of the melt pool is large and the downward heat flow is stabilized [16]. The formation of such <100>//BD-oriented lamellar layers and their associated lamellar boundaries contributes to the strengthening of alloys with excellent ductility [13, 16]. However, in materials such as tungsten, which demonstrates significant brittleness at its grain boundaries, the formation of <100>//BD lamellae must be prevented because lamellar boundaries serve as crack initiation and propagation points. As mentioned above, the density and flowability of the starting powders directly influence the quality of the final product, including its densification and mechanical properties. At present, the development of powders that can achieve improved product quality is being vigorously pursued [18].

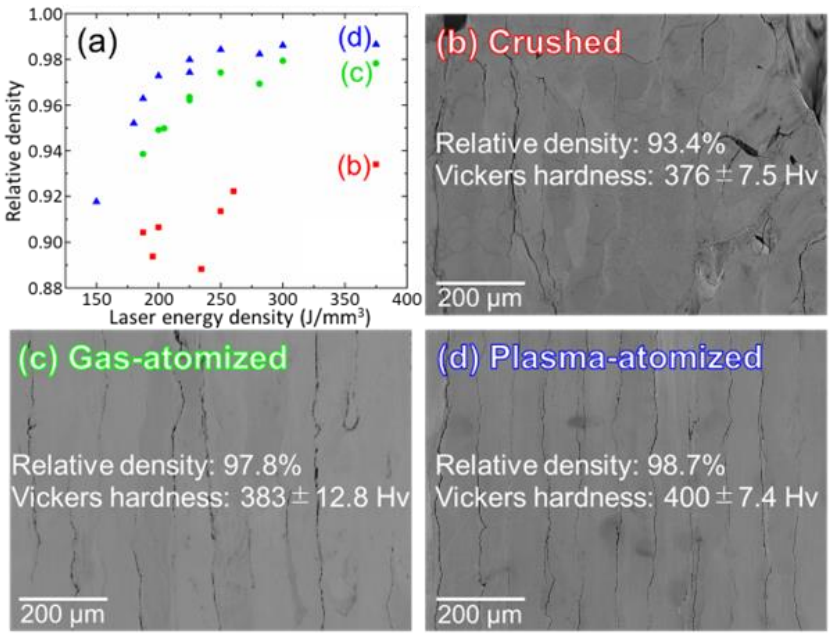

Figure 3. Dependence of product quality on powder properties. (a) Relative density of as-prepared tungsten as a function of the laser energy density. (b–d) SEM images and Vickers hardness of as-prepared products obtained at a laser energy density of 375 J/mm³. Adapted with modifications from reference [12], published under the CC-BY-4.0 license.

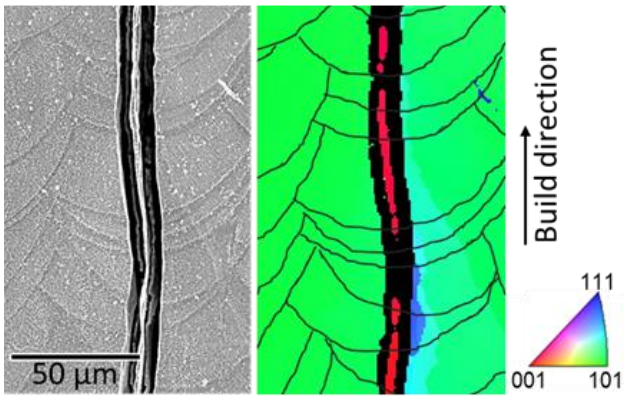

Figure 4. SEM image and corresponding inverse pole figure map of the morphology of the melt pools and crystallographic lamellae observed on the y-z plane in a product fabricated using atomized tungsten powders. <100>//build direction-oriented lamellae occur at the centre of the bottom of the melt pool, with cracks on both sides (high-angle grain boundaries).

3. Control of crystallographic texture formation by PBF method

The crystallographic texture (distribution and accumulation of crystalline orientation) of a material is an important metallurgical factor that controls both its mechanical properties such as strength, ductility, Young's modulus, and wear resistance, as well as its functional properties such as magnetism and corrosion resistance. Therefore, high functionality can be achieved in

anisotropic structures by the suitable control of their crystallographic orientation [19]. Crystallographic texture can be mainly altered between two strategies: formation of randomly oriented polycrystals to obtain isotropic properties and formation of either single-crystalline-like or fiber textures (columnar crystals) to obtain anisotropic properties. These structures must be freely controlled to enable the preparation of high-performance materials. Fortunately, AM has recently been shown to be a promising method for realizing such control.

The development of the crystallographic texture of a material is governed by the superposition of the crystallographic features of the material itself, such as the preferred direction of crystal growth and its multiplicity and symmetry, and the solidification behavior associated with the process conditions, such as solidification in a melt pool (temperature gradient of the solid–liquid interface, movement speed of the solid–liquid interface), melt pool shape, and heat flow direction. The following sections discuss the development of crystallographic texture in LPBF-processed materials depending on the solidification conditions, melt-pool properties, and crystallographic features.

3.1 Single- and polycrystal formation depending on the solidification conditions

In general, when forming single crystals, the temperature gradient G at the solid–liquid interface is increased and the solid–liquid interface velocity (crystal growth rate) R is decreased to suppress compositional undercooling and control the solidification conditions outside the columnar-equiaxed transition (CET) line. Recent digital twin engineering simulations have predicted that the solidification conditions in LPBF are located near the CET line [20, 21]. In other words, single or polycrystals can be produced by precisely controlling the solidification conditions according to the laser properties, such as the laser power P and scanning speed v, during fabrication.

Figure 5 shows the formation of single-crystalline-like and polycrystalline textures in β-type titanium alloys considering the CET drawn with black line indicating change in grain morphology associated with solidification rate (G/R) and the relationship between the laser conditions and solidification conditions [22]. Condition A has a higher energy density, higher power, and lower velocity than Condition B. The G–R distribution under Condition A, in which a single-crystalline-like structure is produced, is on the lower R side than that under Condition B, in which a polycrystal-like structure is formed. This result indicates that Condition A is a solidification condition under which smooth interfacial growth is relatively easy to achieve. Analyses of the effects of P and v on G and R using temperature-field simulations and statistical methods have shown that higher P and v decrease and increase R, respectively, but have no significant effect on G [22].

The position of the CET line depends on material-specific properties, such as the solidus–liquidus temperature difference and nucleation density of the solid phase. However, the laser conditions and tendency of various metallic materials to form single-crystalline or polycrystalline textures coincide [14-17]. When the laser conditions are adjusted to the range in which a single-crystalline-like texture can be formed, the crystallographic orientation can be controlled, depending on the melt pool properties and material type.

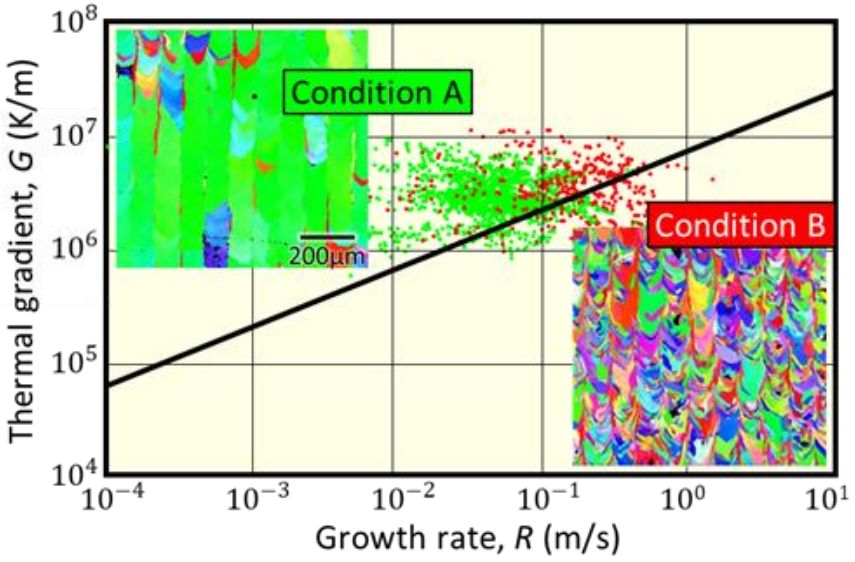

Figure 5. Single-crystalline-like and polycrystalline texture formation depending on the solidification conditions, which are further determined by the laser properties during laser powder bed fusion. Condition A: 360 W and 1200 mm/s; Condition B: 180 W and 1400 mm/s. Adapted with modifications from reference [22], published under the CC-BY-4.0 license.

3.2 Crystallographic texture formation in cubic structures

The formation of microstructures depends largely on the crystal structure of the starting material. In cubic metals with BCC or FCC structures, the direction of preferential crystal growth during solidification is generally parallel to the <100> plane; therefore, given the rapid cooling employed in PBF, especially LPBF, columnar cellular structures and/or secondary dendrite arrays extending toward the <100> plane are formed in the melt pool. Preferential orientation primarily adopted by the cell growth which is dendrite without secondary arm formation due to fast cooling rate during LPBF. Therefore, the texture formation strongly affiliated to cell orientation.

During solidification in the melt pool, columnar cells aligned to the <100> plane tend to grow parallel to the heat flow direction and perpendicular to the tangential direction of the melt pool [23, 24] if the effect of epitaxial growth is negligible. However, in practice, epitaxial growth occurs from the underlying and adjacent solidification zone [25], and the combination of preferential growth direction, melt pool shape based on the heat flow direction, and crystal orientation at the solidification zone determines the final crystallographic texture and preferred orientation of the obtained material [26]. In other words, the artificial adjustment of these geometrical relationships could enable the control of single-crystalline-like or fiber textures and even their crystal orientations, such as the <100>, <110>, and <111> planes, parallel to the BD. The scan strategy, which refers to the combination of laser scanning directions per layer [3, 4, 27], may be a representative LPBF parameter that can be controlled for this purpose.

Figure 6 shows the scan-strategy dependence of the crystallographic textures of LPBF fabrications of β-titanium alloys and tungsten in terms of inverse pole figure maps and {100} pole diagrams [4, 28]. The preferential grain orientation changes depending on the scan strategy during the LPBF fabrication of β-titanium alloys; specifically, a crystallographic texture with a {110}z<100>x orientation is formed under scan strategy X, and a crystallographic texture with a

{100}z<100>x orientation is formed under scan strategy XY. By contrast, the crystallographic texture of tungsten, which forms a cubic structure, similar to β-titanium alloys, is independent of the scan strategy, forming a {100}z<110>x orientation in the scan strategies X and XY. Moreover, scan strategy X indicated tilted grain morphology towards the scan track direction for tungsten, which can be identified in IPF map and pole figure represented in figure 6.

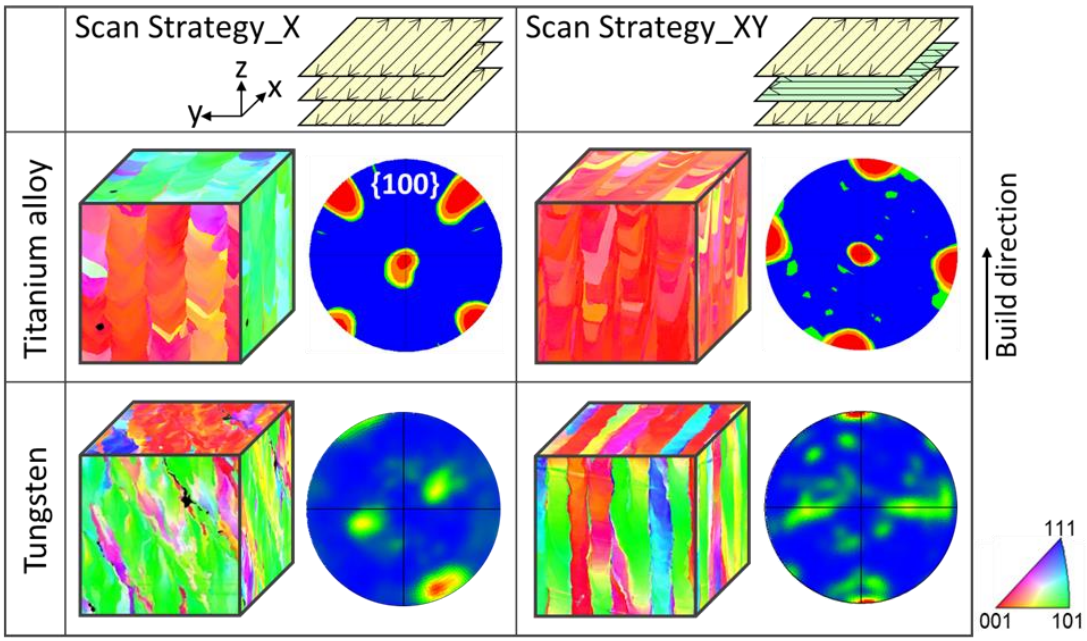

Figure 6. Variation of the formation of crystallographic texture during laser powder bed fusion depending on the starting material (β-titanium alloy or tungsten) and scan strategy (X or XY). Adapted with modifications from references [4] and [28], published under the CC-BY-4.0 license.

The difference in crystallographic texture orientation between the two materials can be attributed to differences in their melt pool shape: the melt pool formed by β-titanium alloys has a long tail, whereas the melt pool formed by tungsten hardly shows this tail and has a hemispherical shape [28]. This difference in melt-pool shape is due to the large difference in the melting point and thermal conductivity between the two materials.

Figure 7(a, b) shows optical microscopy images of the y-z section of the sample surface produced under scan strategies X and XY after chemical etching. A certain melt pool shape and cell structure can be observed owing to the segregation of a small amount of the constituent elements [29]. The direction of cell elongation differs between the left and right sides of the melt pool, each having an angle of approximately ±45° relative to the BD, and the left and right solid–liquid interfaces meet at an angle of approximately 90° at the center of the melt pool (the meeting interface is indicated by the white arrow in the figure). Thus, a grain boundary with a low angle misorientation exists approximately at the center of the melt pool. The crystalline orientation formed during LPBF self-adjusts to reduce the orientation difference at the center of the melt pool, indicating a cell growth interface from the side branches of the melt pool. Therefore, the {110}z<100>x orientation becomes stable, the crystal orientation is transferred to the adjacent melt pool by side-branching or to the next melt pool layer (as indicated by the • in figure 7(a, b)), solidification occurs at the melt pool boundary, and the growth direction of the cell changes by 90° and maintains its crystal orientation [25].

Although epitaxial growth under scan strategy XY is possible, it results in a different crystal orientation. The laser scanning direction in scan strategy XY alternates from the x direction (where <100>//x and <011>//y are the stable orientations in the melt pool) to the y direction (where <100>//y and <011>//x are the stable orientations) such that the <100> plane in the solidification zone and the <011> plane in the front layer compete in texture formation depending on the laser scanning direction. Because the growth rate of the <100> plane is greater than that of the <011> plane [30], the <100> plane is first oriented in the two scanning directions (x and y directions), followed by the z direction, stabilizing the {001}z<100>x crystallographic texture. The crystal orientation selection of the adjacent melt pool and subsequent layer is driven by the reduction in the crystal orientation difference at the solid–liquid interface in the transverse section of the melt pool.

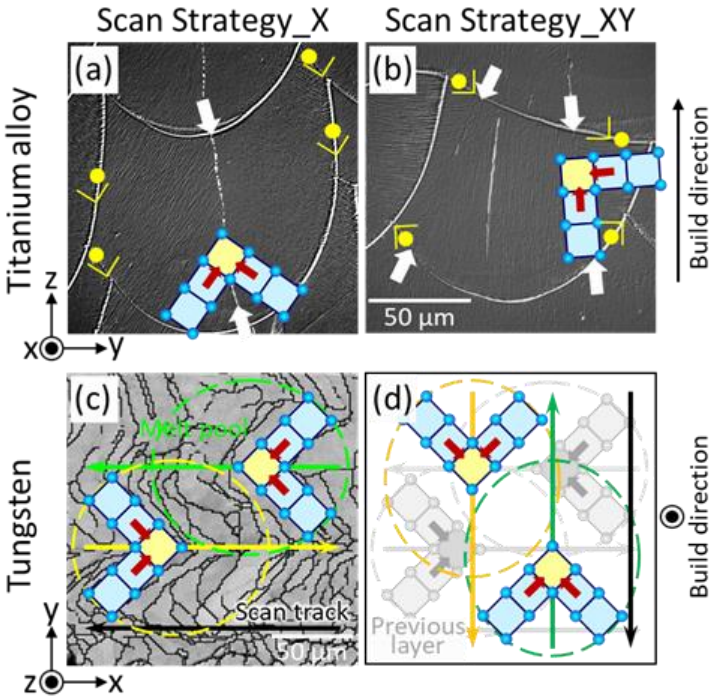

Figure 7. Melt pool shape, solidification plane, and <100> growth direction on this plane in titanium alloy and tungsten. Adapted with modifications from references [4] and [28], published under the CC-BY-4.0 license.

Solidification is known to occur on the x-y plane in hemispherical melt pools of tungsten [28]. In pure metals, no segregation occurs; therefore, the direct observation of the cell and melt-pool shape is not possible. However, the direction of solidification can be estimated from the grain geometry and temperature-field simulations. Scan strategy X results in <100> growth in the x-y plane at an angle of ±45° with respect to the laser scanning direction owing to the direction of *G*, forming a crystal orientation of {100}z<110>x, as shown in figure 7(c). In this case, the crystal growth direction in the subsequent layer corresponds to that in the previously melted layer in scan strategy XY, as shown in figure 7(d), and no change in the direction of the crystal orientation occurs between the two scan strategies[2] [28].

The melt pool shape varies with the physical properties of metallic materials; however, the melt pool shape and resulting crystallographic texture orientation also vary depending on the laser scanning conditions and energy distribution of the heat source [31-33].

3.3 Crystallographic orientation formation in hexagonal crystal structures

Materials with a hexagonal crystal structure show a crystallographic texture that completely differs from that of materials with a cubic crystal structure; figure 8 shows the scan-strategy dependence of the crystallographic texture of intermetallic $NbSi_2$, which has a hexagonal C40 structure [34]. This hexagonal intermetallic compound shows preferential growth in the <0001> direction. The multiplicity of the <100> plane in the cubic crystal system is three if the positive and negative directions are not distinguished; by contrast, the multiplicity of the <0001> plane in the hexagonal crystal system is one and shows low symmetry. In other words, the crystalline orientation around the <0001> direction is ambiguous and arbitrary, and a single-crystalline-like microstructure is not achieved, although fiber texture formation with a <0001> orientation parallel to the BD occurs. Because the crystal orientation around the <0001> orientation is not determined, a similar crystallographic texture develops independently of scan strategy [34], as shown in figure 8, while scan strategy X for $NbSi_2$, exhibited similar tilted grain, similar to the case of tungsten, towards scan track direction.

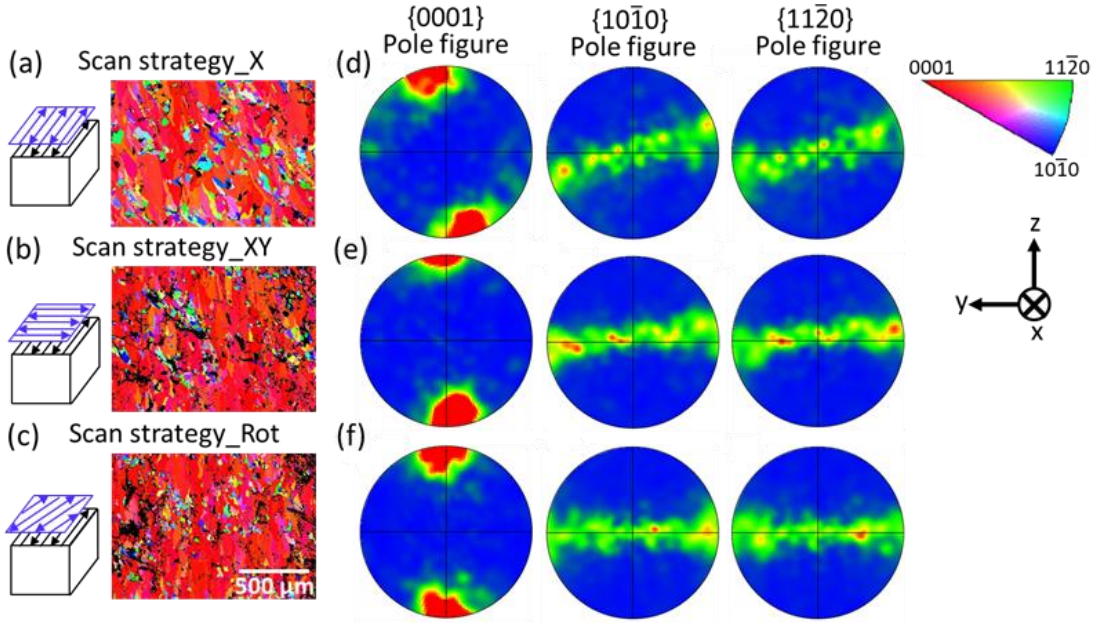

Figure 8. Dependence of crystallographic texture formation in hexagonal $NbSi_2$ on the laser bed powder fusion scan strategy. Adapted with modifications from reference [34], published under the CC-BY-4.0 license.

However, even in the case of hexagonal crystal systems, single-crystalline-like textures can be successfully formed by applying a special scan strategy that takes symmetry into account [35]. The formation behaviors of the crystallographic textures of cubic and hexagonal crystal systems are summarized in figure 9.

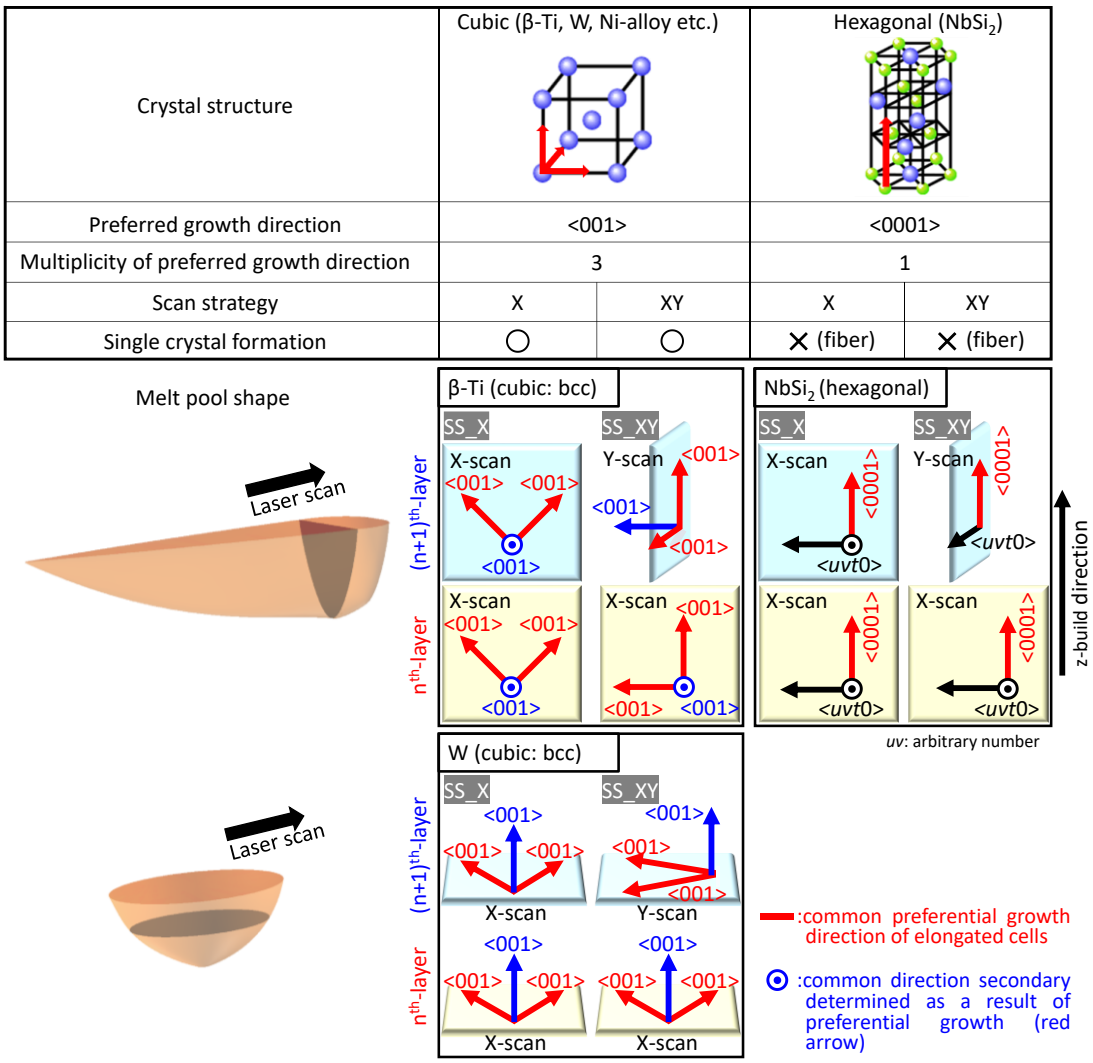

Figure 9. Relationships among crystal structure, preferential growth direction, and texture formation under scan strategies X and XY during laser powder bed fusion. Adapted with modifications from reference [34], published under the CC-BY-4.0 license.

4. Alloy design for the preparation of single-crystalline-like biological high-entropy alloys by laser powder bed fusion

AM realizes unique microstructures and functionalities in existing alloys that cannot otherwise be obtained via conventional methods by employing a unique thermal history, such as ultrarapid cooling and reheating in track-by-track and layer-by-layer melt pools [16, 36, 37]. Future research and development efforts will focus on creating novel functionalities by designing alloys that are tailored to the characteristics of AM to realize their maximum potential[2].

Our research group developed a quintic $(TiZr)_{30.43}(NbTaMo)_{13.04}$ BioHEA with a BCC crystal structure as a new bone biomaterial [38, 39]. By utilizing ultrarapid LPBF cooling to suppress segregation, which cannot be avoided in casting (figure 10(b)), and maximize solid-solution strengthening, we obtained an ultrahigh-strength metal material with good biocompatibility [40].

However, a low Young's modulus, which is essential for biomaterials used in bones, must be achieved to avoid stress shielding.

To achieve a low Young's modulus, we attempted to simultaneously (1) reduce the number of total electrons (VEC) per atom in the valence band and (2) achieve Young's modulus anisotropy (low Young's modulus at <100>) via single-crystalline-like texture formation [41]. Single-crystalline-like texture formation was not observed in the aforementioned quintic alloy (figure 10(d)) because segregation could not be completely suppressed even under ultrarapid cooling during LPBF, resulting in dendrite formation (figure 10(c)). Moreover, high-melting-point dendrites remained in the melt at the bottom of the melt pool, forming heterogeneous nucleation sites and generating equiaxed grains (figure 10(d)), which are detrimental to the formation of a single-crystalline-like texture [40]. To avoid the formation of equiaxed grains, we designed the composition of $(TiZrHf)_{28.33}(NbTa)_{6.74}Mo_{1.55}$ to satisfy condition (1) while reducing the temperature range (ΔT) in the solid–liquid coexistence region and the deviation of the equilibrium distribution coefficient from 1 (figure 10(e)), thus suppressing the segregation tendency of the alloy [41]. ΔT was reduced from approximately 400 to 50 K and VEC was reduced from 4.52 to 4.17, both of which are significantly reductions. As a result, as shown in figure 10(h), no equiaxed grains were formed at the melt boundary owing to segregation, and a {100}z<100>x single-crystalline-like texture similar to that of the β-type titanium alloy shown in figure 6 was successfully obtained under scan strategy XY. The single-crystalline-like textured BioHEA fabricated by LPBF exhibited a yield strength greater than 1350 MPa, which is approximately 1.4 times greater than that of the cast material, a low Young's modulus of less than 90 GPa, and biocompatibility equivalent to that of pure Ti [41]. Thus, a useful metal biomaterial with multiple functionalities was obtained. These results provide a good example of the preparation of highly functional materials by utilizing the specific characteristics of LPBF.

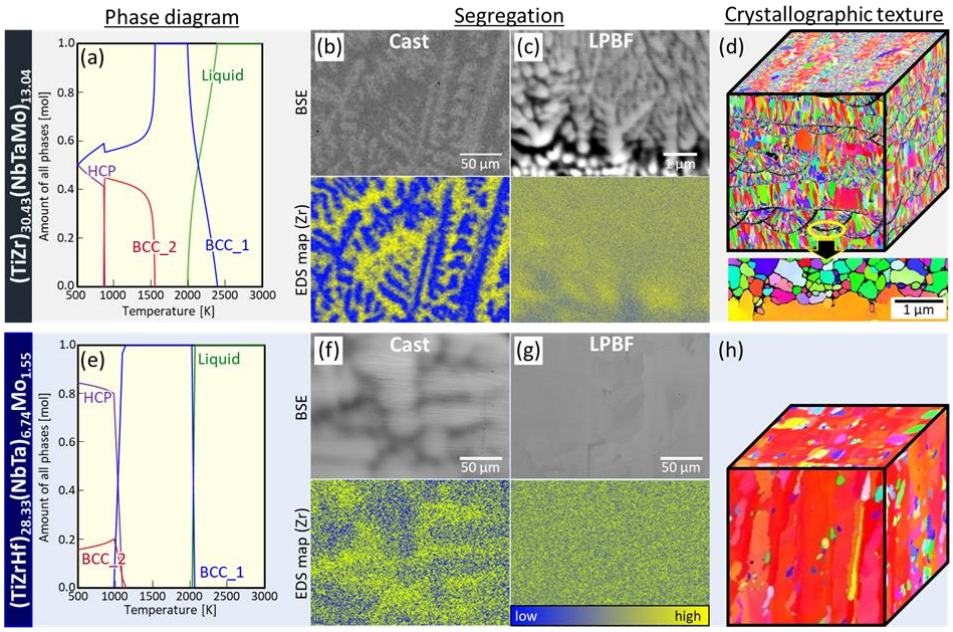

Figure 10. Alloy design for the creation of biological high-entropy alloys (BioHEAs) with a single-crystalline-like texture. (a–d) Alloy with segregation and failed single-crystalline texture formation. (e–h) BioHEA with a single crystalline-like texture formed by suppressing segregation via alloy design. Adapted with modifications from references [40] and [41], published under the CC-BY-4.0 license.

5. Summary and future recommendations

This article reviews recent findings on the control of material microstructures exhibiting anisotropic properties by metal AM, particularly LPBF. Various crystallographic texture formation mechanisms have been reported for a wide range of materials, but the artificial and flexible control of such microstructures has not yet been fully established. In particular, the control of crystallographic textures in materials that undergo solid–solid transformation, including Ti alloys [42] and TiAl [43] containing an α-phase such as Ti-6Al-4V and martensitic stainless steels [44], requires the control of not only the crystal orientation during solidification but also the variant selection during phase transformation. The latter is a challenging issue because it requires limiting the selectivity of the variants during phase transformation, in addition to controlling the crystal orientation during solidification. Many materials and products made from materials in which the crystal orientation is directly related to their functionality, including metals, ceramics, and polymers, have been reported. Control of microstructure with anisotropic properties is expected to become a major guideline for future research and development efforts in AM. Moreover, design aspects from the viewpoint of material control, in addition to shape control, are expected become increasingly important.

Acknowledgements

This work was supported by a Grant-in-Aid for Scientific Research (JP23H00235) from the Japan Society for the Promotion of Science (JSPS) and by CREST-Nanomechanics: Elucidation of macroscale mechanical properties based on understanding the nanoscale dynamics of innovative mechanical materials (Grant Number: JPMJCR2194) from the Japan Science and Technology Agency (JST).

References

[1] Kodama H 1981 *Rev. Sci. Instrum*. **52** 1770
[2] Clare A T, Mishra R S, Merklein M, Tan H, Todd I, Chechik L, Li J, Bambach M 2022 *J. Mater. Proc. Technol.* **299** 117358
[3] Sun S-H, Hagihara K, Nakano T 2017 *Mater. Des*. **140** 307
[4] Ishimoto T, Hagihara K, Hisamoto K, Sun S-H, Nakano T 2017 *Scr. Mater*. **132** 34
[5] Ishimoto T, Nakano T 2022 *J. Jpn. Inst. Light Metals* **72** 327
[6] Nakano T *et al* 2024 Materia **63** 36
[7] Nakayama H, Yamagami K, Kyogoku H, Komatsu S 1997 *J. Jpn. Soc. Powder Powder Metall.* **44** 427
[8] Shinagawa K 2019 *J. Jpn. Soc. Powder Powder Metall.* **66** 387
[9] Vock S, Klöden B, Kirchner A, Weißgärber T, Kieback B 2019 *Prog. Addit. Manuf*. **4** 383
[10] Zhou X, Liu X, Zhang D, Shen Z, Liu W 2015 *J. Mater. Proc. Technol*. **222** 33
[11] Li K-L, Chen J-H, Zhao C-C, Shen Z-J, Liu W 2021 *Tungsten* **3** 218
[12] Gokcekaya O, Ishimoto T, Todo T, Wang P, Takayoshi N 2021 *Addit. Manuf. Lett*. **1** 100016
[13] Sun S-H, Ishimoto T, Hagihara K, Tsutsumi Y, Hanawa T, Nakano T 2019 *Scr. Mater*. **159** 89
[14] Ishimoto T, Wu S, Ito Y, Sun S-H, Amano H, Nakano T 2020 *ISIJ Int*. **60** 1758
[15] Tsutsumi Y, Ishimoto T, Oishi T, Manaka T, Chen P, Ashida M, Doi K, Katayama H, Hanawa T, Nakano T 2021 *Addit. Manuf*. **45** 102066
[16] Gokcekaya O, Ishimoto T, Hibino S, Yasutomi J, Narushima T, Nakano T 2021 *Acta Mater*. **212** 116876
[17] Hibino S, Todo T, Ishimoto T, Gokcekaya O, Koizumi Y, Igashira K, Nakano T 2021 *Crystals* **11** 1064
[18] Sugitani Y 2021 *J. Jpn. Thermal Spray Soc*. **58** 154
[19] Hagihara K, Nakano T 2022 *JOM* **74** 1760
[20] Miyata Y, Okugawa M, Koizumi Y, Nakano T 2021 *Crystals* **11** 856
[21] Koizumi Y, Okugawa M 2022 *ISIJ Int*. **62** 2183
[22] Ishimoto T, Suganuma R, Nakano T 2023 *Mater. Lett*. **349** 134835

[23] Ekubaru Y, Gokcekaya O, Ishimoto T, Sato K, Manabe K, Wang P, Nakano T 2022 *Mater. Design* **221** 110976
[24] Ishimoto T *et al* 2021 *Scr. Mater*. **194** 113658
[25] Pham M-S, Dovgyy B, Hooper P A, Gourlay C M, Piglione A 2020 *Nat. Commun*. **11** 749
[26] Ishimoto T, Hagihara K, Hisamoto K, Nakano T 2021 *Addit. Manuf*. **43** 102004
[27] Marattukalam J, Karlsson D, Pacheco V, Beran P, Wiklund U, Jansson U, Hjörvarsson B, Sahlberg M 2020 *Mater. Design* **193** 108852
[28] Todo T, Ishimoto T, Gokcekaya O, Oh J, Nakano T 2022 *Scr. Mater*. **206** 114252
[29] Okugawa M, Saito K, Yoshima H, Sawaizumi K, Nomoto S, Watanabe M, Nakano T, Koizumi Y 2024 *Addit. Manuf*. **84** 104079
[30] Messler RW 2008 *Principles of Welding* (New York: Wiley)
[31] Liu Y, Nose K, Okugawa M, Koizumi Y, Nakano T 2023 *Mater. Trans*. **64** 1135
[32] Sun S-H, Hagihara K, Ishimoto T, Suganuma R, Xue Y-F, Nakano T 2021 *Addit. Manuf*. **47** 102329
[33] Bi J, Wu L, Li S, Yang Z, Jia X, Starostenkov M D, Dong G 2023 *J. Mater. Res. Technol*. **26** 4606
[34] Hagihara K, Ishimoto T, Suzuki M, Ozasa R, Matsugaki A, Wang P, Nakano T 2021 *Scr. Mater.* **203** 114111
[35] Ozasa R, Kizawa Y, Hagihara K, Sato K, Tobata T, Tokunaga T, Nakano T 2024 Mater Des submitted
[36] Yang J, Yu H, Yin J, Gao M, Wang Z, Zeng X 2016 *Mater. Des*. **108** 308
[37] Todai M, Nakano T, Liu T, Yasuda H Y, Hagihara K, Cho K, Ueda M, Takayama M 2017 *Addit. Manuf*. **13** 61
[38] Todai M, Nagase T, Hori T, Matsugaki A, Sekita A, Nakano T 2017 *Scr. Mater*. **129** 65
[39] Iijima Y, Nagase T, Matsugaki A, Wang P, Ameyama K, Nakano T 2021 *Mater. Des*. **202** 109548
[40] Ishimoto T *et al* 2021 *Scr. Mater*. **194** 113658
[41] Gokcekaya O *et al*. 2023 *Mater. Res. Lett*. **11** 274
[42] Amano H, Ishimoto T, Suganuma R, Aiba K, Sun S-H, Ozasa R, Nakano T 2021 *Addit. Manuf*. **48** 102444
[43] Park S-H, Gokcekaya O, Ozasa R, Oh M-H, Kim Y-W, Kim H-S, Nakano T 2023 *Met. Mater. Int*. **30** 1227
[44] Kannan R, Nandwana P 2022 *Sci. Rep.* **12** 6396